Journal of Alloys and Compounds 582 (2014) 12–21

Contents lists available at ScienceDirect

Journal of Alloys and Compounds

journal homepage: www.elsevier.com/locate/jalcom

Sonicated sol–gel preparation of nanoparticulate ZnO thin films with various deposition speeds: The highly preferred *c*-axis (002) orientation enhances the final properties

M.F. Malek [a,*], M.H. Mamat [a], Z. Khusaimi [b], M.Z. Sahdan [c], M.Z. Musa [a], A.R. Zainun [d], A.B. Suriani [e], N.D. Md Sin [a], S.B. Abd Hamid [f], M. Rusop [a,b]

[a] NANO-ElecTronic Centre (NET), Faculty of Electrical Engineering, Universiti Teknologi MARA (UiTM), 40450 Shah Alam, Selangor, Malaysia
[b] NANO-SciTech Centre (NST), Institute of Science (IOS), Universiti Teknologi MARA (UiTM), 40450 Shah Alam, Selangor, Malaysia
[c] Microelectronic & Nanotechnology Centre (MiNT), Universiti Tun Hussein Onn Malaysia (UTHM), 86400 Batu Pahat, Johor, Malaysia
[d] Faculty of Electrical & Electronics Engineering, Universiti Malaysia Pahang (UMP), Lebuhraya Tun Razak, 26300 Kuantan, Pahang, Malaysia
[e] Department of Physics, Faculty of Science and Mathematics, Universiti Pendidikan Sultan Idris, 35900 Tanjung Malim, Perak, Malaysia
[f] Nanotechnology and Catalysis Research Centre (NANOCAT), Universiti Malaya (UM), 50603 Kuala Lumpur, Malaysia

ARTICLE INFO

Article history:
Received 24 March 2013
Received in revised form 31 July 2013
Accepted 31 July 2013
Available online 8 August 2013

Keywords:
ZnO
Thin films
Sol–gel processes
X-ray diffraction
Strain

ABSTRACT

Zinc oxide (ZnO) thin films have been deposited onto glass substrates at various deposition speeds by a sonicated sol–gel dip-coating technique. This work studies the effects of deposition speed on the crystallisation behaviour and optical and electrical properties of the resulting films. X-ray diffraction (XRD) analysis showed that thin films were preferentially oriented along the (002) *c*-axis direction of the crystal. The transformation sequence of strain and stress effects in ZnO thin films has also been studied. The films deposited at a low deposition speed exhibited a large compressive stress of 0.78 GPa, which decreased to 0.43 GPa as the deposition speed increased to 40 mm/min. Interestingly, the enhancement in the crystallinity of these films led to a significant reduction in compressive stress. All films exhibited an average transmittance of greater than 90% in the visible region, with absorption edges at ~380 nm. The photoluminescence (PL) measurements indicated that the intensity of the emission peaks varied significantly with deposition speed. The optical band gap energy (E_g) was evaluated as 3.276–3.289 eV, which increased with decreasing compressive stress along the *c*-axis. The energy band gap of the resulting ZnO films was found to be strongly influenced by the preferred *c*-axis (002) orientation.

1. Introduction

Zinc oxide (ZnO) materials have recently attracted tremendous attention among researchers due to their wide range of electrical and optical properties. ZnO is a II–VI semiconductor with a wide and direct band gap (3.2–3.4 eV at 300 K), excellent chemical and thermal stability, and the unique electrical and optoelectronic property of a large exciton binding energy (60 meV), which could lead to lasing action even above room temperature [1–3]. Furthermore, its tunable band gap and high transparency have made ZnO a candidate material for short-wavelength and transparent optoelectronic devices including light-emitting diodes (LEDs) [4,5], solar cells [6], and sensors [7]. These properties and potential applications make this material an excellent subject for theoretical and experimental studies. Generally, ZnO thin films grow as *n*-type semiconductors due to their native defects. To achieve ZnO-based devices with the desired characteristics, high quality *n*-type ZnO thin films must be fabricated. It is convenient to grown-type ZnO thin films with good electrical properties, as ZnO possesses intrinsic electron conductivity due to its oxygen vacancies (V_o) and interstitial zinc ions (Zn_i), which act as donors in the crystal lattice. It is well known that the adsorption and desorption of oxygen on the ZnO surface and grain boundaries lead to significant decreases and increases in the conductivity of ZnO polycrystalline thin films.

ZnO films can be produced in various phases such as wurtzite (hcp), rocksalt (fcc), cesium chloride (sc), and zinc blend (fcc) [8,9]. Under ambient conditions, ZnO crystallises in the wurtzite structure, a tetrahedrally coordinated structure with a hexagonal lattice. ZnO films can crystallise in various orientations as a function of the deposition technique, sol concentration and other factors. A higher *c*-axis (002) peak orientation indicates the minimisation of the internal stress and free surface energy of the films, as well as dense atomic packing. The quality of the film is typically determined by its crystalline orientation, surface uniformity, transparency and conductivity [10,11]. Among all of these parameters, the crystalline orientation is the key to achieving a ZnO thin film with piezoelectric properties.

---

[*] Corresponding author. Tel.: +60 176027671.
E-mail address: firz_solarzelle@yahoo.com (M.F. Malek).

0925-8388/$ - see front matter © 2013 Elsevier B.V. All rights reserved.
http://dx.doi.org/10.1016/j.jallcom.2013.07.202

Strong preferential growth of ZnO nanocrystals along the *c*-axis (002) plane suggests a wurtzite structure due to the minimisation of the surface free energy of each crystal plane [12]. Therefore, many researchers have studied the influence of deposition parameters on the final properties of ZnO thin films, particularly the crystal orientation. Bouderbala et al. prepared ZnO films by r.f. sputtering [13], varying the deposition time to obtain different thicknesses. Their results suggest that the crystallinity is improved when the film thickness increases. On the other hand, XRD analysis showed that the grains were always oriented according to the *c*-axis perpendicular to the substrate surface, regardless of the thickness. Ozga and co-workers investigated the photo-induced second harmonic generation (SHG) in Au nanoparticle-deposited ZnO nanocrystallite films using coherent bicolour interactions [14]. They found that increasing gold nanoparticle content favours an enhancement of the output SHG, while the maximum second order optical susceptibility was achieved due to the enhancement of the electron–phonon interactions at the interfaces of the nanocrystallites [14,15]. The SHG depended on the degree of crystallinity, grain boundaries and film interfaces. The deposition of hexagonal films with the crystallographic *c*-axis between the substrate planes enhanced the susceptibility [14].

Recent studies have reported modifications to these (002) oriented thin films to enhance their final properties. Shabannia and Abu Hassan produced ZnO nanorods by a low-temperature chemical bath deposition on a ZnO/PS substrate [16]. The ZnO nanorods exhibited a high crystallinity with hexagonal wurtzite phases, grew vertically in the (002) direction along the *c*-axis, and exhibited a low compressive strain (-0.0363%) along this axis. Salam et al. prepared intrinsic and aluminum-doped zinc oxide thin films via spin coating over soda-lime glass substrates [17]. They reported that further increasing the Al doping level to 2 at.% caused a lattice distortion due to the difference in the crystallite size between Al and Zn, along with a slight decrease in the preferred (002) orientation. Drmosh et al. developed Cu-doped ZnO (ZnO:Cu) thin films on a glass substrate at room temperature by a pulsed laser deposition (PLD) method [18]. All of the ZnO:Cu films preferentially oriented along the (002) crystal plane. These authors claimed that the ZnO:Cu films exhibited a leftward shift in the (002) peak and a decreased intensity of this peak as the Cu concentration was increased. In our previous paper [19], we reported that ZnO films strongly oriented along the (002) plane can be prepared on glass substrates by a dip-coating technique. The sol concentration significantly affected the crystal orientation/behaviour and other properties of the final films. Furthermore, a nearly stress- and strain-free thin film was obtained for the film deposited in a highly *c*-axis oriented direction along the (002) plane. Moreover, a higher degree of crystallinity along the (002) plane improved the performance of the fabricated solar cell [20]. The solar cell device based on Al:ZnO nanorod arrays (highly *c*-axis oriented) exhibited an efficiency, η, of 0.287%, compared with 0.263% for the device based on ZnO nanorod arrays (low *c*-axis orientation). The current study describes the growth process and the effects of the deposition speed on the crystal orientation as well as the optical and electrical properties of the films. This study also provides a deep understanding of the nanoparticulate growth to obtain more detailed insight into the conditions for the formation of highly *c*-axis oriented ZnO films.

2. Experimental procedures

2.1. Materials preparation

The ZnO sonicated sol–gel was prepared as follows: zinc acetate dihydrate ($Zn(CH_3COO)_2 \cdot 2H_2O$) was first dissolved in 2-methoxyethanol ($C_3H_8O_2$) at room temperature. Then, monoethanolamine (MEA, C_2H_7NO) was added as a sol stabiliser. The molar ratio of MEA to zinc acetate was maintained at 1.0, and the concentration of zinc acetate was 0.4 mol/L. The resulting solution was stirred at 80 °C for 1 h to yield a clear and homogeneous solution, which served as the coating solution. Afterwards, the solution was sonicated at 50 °C for 1 h using an ultrasonic water bath (Hwasin Technology Powersonic 405, 40 kHz). Finally, the solution was aged for 24 h before the deposition process. Corning 7740 glass (20×20 mm^2) was used as the substrate material. The glass sheets were cleaned twice in an ultrasonic bath with sequences of acetone (5 min), methanol (5 min), and deionised water (5 min). The substrates were subsequently dried by a stream of nitrogen gas and preserved in a desiccator.

2.2. Film growth deposition

The ZnO films were deposited by dipping a glass substrate into the coating solution and withdrawing it at rates of 10–50 mm/min at room temperature. To facilitate film thickness measurements, a section of the substrate was covered with adhesive tape, which was subsequently peeled off after the deposition process. The substrates were then heated in a furnace at 300 °C for 10 min to evaporate the solvent and remove residual organic material. Each sample was subjected to this procedure five times to obtain an initial five layer film structure. After coating the required number of layers, the ZnO thin film was annealed at 500 °C for 1 h before cooling in air to room temperature. Fig. 1 presents a diagram of the sol preparation and deposition process.

2.3. Characterisation

The degree of crystallinity and crystalline orientation of the ZnO thin films was measured using a Bruker AXS D8 Advance X-ray diffractometer (XRD) with Cu Kα radiation, $\lambda = 1.54$ Å. The beam voltage and beam current were 40 kV and 40 mA, respectively. The scan pattern data were collected in a standard θ–2θ Bragg–Brentano geometry configuration between 25° and 60° with a step length of 0.02°. The surface morphology of the films was evaluated using a ZEISS Supra 40VP field emission scanning electron microscope (FESEM) with an operating voltage between 0.02 and 30 kV. The film thickness was measured using a KLA Tencor P-6 profilometer. UV–Vis–NIR spectroscopy was performed using a Varian Cary 5000 UV–Vis–NIR spectrophotometer over the wavelength range between 300 and 1500 nm with a data interval of 1 nm. The photoluminescence (PL) properties of the synthesised film were measured using a Horiba Jobin Yvon-79 DU420A-OE-325 PL spectrophotometer with a helium–cadmium (He–Cd) excitation laser source operating at 325 nm. The electrical properties were characterised by sheet resistance measurements with a two-probe DC system and an Advantest R6243 power supply. Gold (Au) was sputtered as an electrode for current–voltage (*I*–*V*) measurements using an EMITECH K550X sputter coater. The *I*–*V* curve of the film was tested to verify the suitability of the deposited films for use in electronic devices.

3. Results and discussion

3.1. Structural and morphological characterisation

The deposition speed was investigated because the pulling rate affects the surface morphology and the film thickness. The XRD patterns of the ZnO thin film for each deposition speed are presented in Fig. 2. The presence of all peaks was indexed to the standard XRD spectrum of the ZnO structure in accordance with JCPDS card No. 00-036-1451. All films exhibited a main peak attributed to the (002) plane. Other peaks represent low intensity (100) and (101) diffraction peaks. The adhesion of the ZnO thin film to the glass substrate was examined by an ordinary tape peel test using 3M Scotch Tape™. None of the films deposited on glass substrates appeared to be removed, indicating strong adherence of the films to the glass substrates. Brinker and Scherer claimed that lower deposition speeds produce thinner films because the solvent can more easily evaporate from the film [21,22]. As a result, oriented grain growth may easily occur in the second layer because of the presence of slightly oriented grains in the previous layer. Therefore, the strongest preferential orientation along the *c*-axis is observed at $2\theta = 34.56°$ for ZnO films deposited at 40 mm/min, which indicates the existence of single phase ZnO with a hexagonal wurtzite structure. The peaks other than that of the (002) plane are very weak. Therefore, the crystallites are highly oriented along the *c*-axis, which is perpendicular to the substrate. Increasing the deposition speed to 50 mm/min resulted in a slight decrease in the (002) peak intensity. At higher deposition speeds, the thickness of the film per dip became thicker, and it became more difficult for the solvent to evaporate, which could disturb the ori-

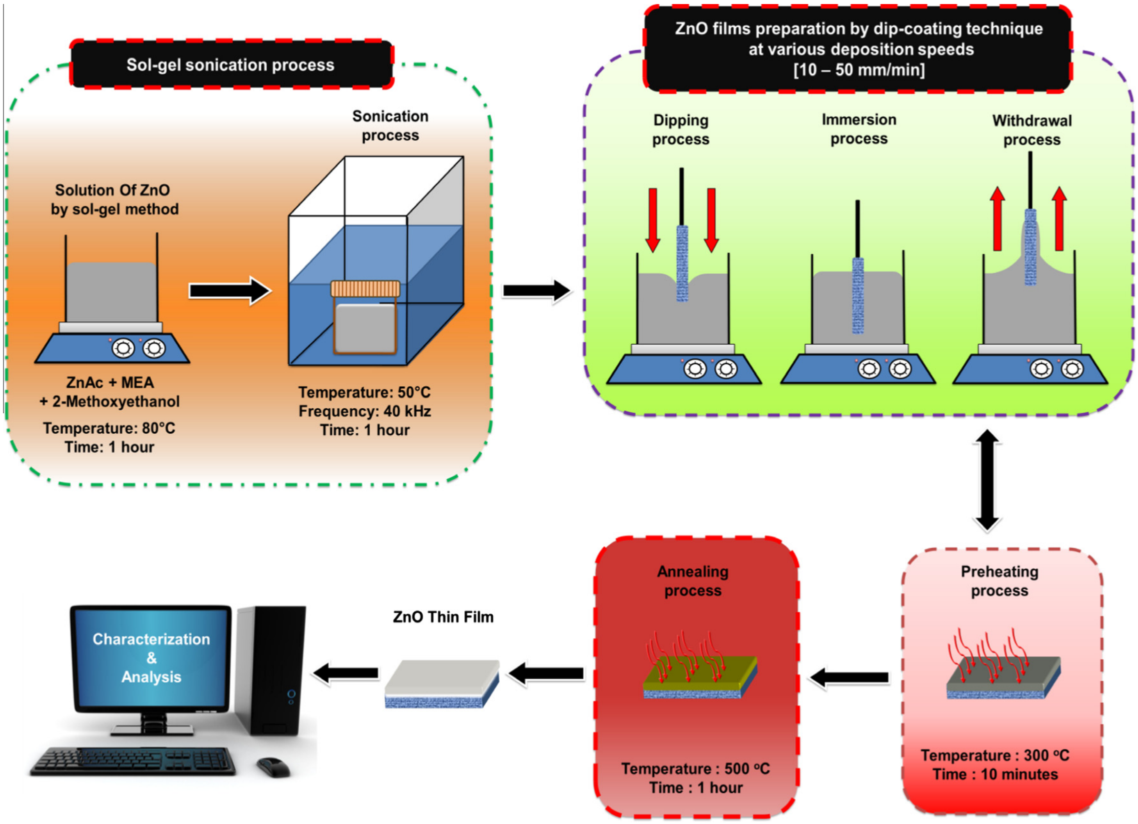

Fig. 1. Schematic diagram of ZnO thin film preparation procedure at various deposition speeds.

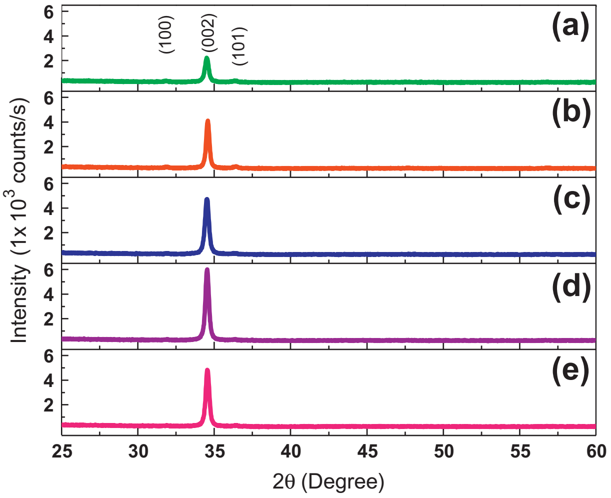

Fig. 2. XRD patterns of ZnO thin films prepared at various deposition speeds: (a) 10 mm/min, (b) 20 mm/min, (c) 30 mm/min, (d) 40 mm/min and (e) 50 mm/min.

ented crystal growth [23]. The thin film deposited at 10 mm/min was characterised by a broad, poorly defined XRD peak along the (002) plane orientation, indicating a low degree of order as is typical for an amorphous or nanocrystalline material. These results indicate that the ZnO thin film does not grow well at a lower deposition due to an insufficient amount of the Zn^{2+} species, resulting in slower ZnO growth than films grown at higher deposition speeds [24,25]. The degree of *c*-axis orientation for ZnO thin films is strongly dependent on the initial zinc concentration [26,27]. This finding is also supported by the work of Shinde et al., who proved that zinc content has a significant effect on ZnO growth along the (002) plane [28]. These results indicate the possibility of producing a highly preferred orientation along the *c*-axis plane by controlling the deposition speed of the substrate. The relative peak intensity of the film was measured from its XRD pattern using the following formula (1) [29]. The relative peak intensity orientation $P_{(hkl)}$ of a particular plane (*hkl*) can be written as

$$\mathrm{P}_{(\mathrm{hkl})} = \frac{I_{(hkl)}}{\sum I_{(hkl)}} \tag{1}$$

where $I_{(hkl)}$ is the (*hkl*) peak intensity and $\sum I_{(hkl)}$ is the sum of the intensities of all the diffraction peaks of the ZnO thin film deposited on a glass substrate. The relative peak intensity of the (002) plane is calculated in Table 1. The wurtzite hexagonal phase of ZnO has a natural tendency to grow along the (002) plane, which has a minimum surface energy. This finding was supported by Zhang et al., who reported that the minimisation of surface energy favours a (002) textured ZnO film [30–32]. The average crystallite sizes of the films deposited at various deposition speeds have been calculated using Scherrer's equation, presented below [33–35]:

$$\mathrm{D} = \frac{0.94\lambda}{\beta\cos\theta} \tag{2}$$

where λ, β and θ are the X-ray wavelength (1.54 Å), the Bragg's diffraction angle in degrees and the full width at half maximum (FWHM) of the peak corresponding to the "θ" value in radians, respectively. The average crystallite sizes of the films are listed in Table 1. The crystallite size increased from 26 to 32 nm as the deposition speed was increased from 10 to 50 mm/min. Moreover, the XRD stack diagrams in Fig. 2 show that the position of the (002) diffraction peak shifted towards the bulk ZnO peak as the deposition speed increased to 40 mm/min, indicating the relaxation of the crystal lattice structure, thus minimising the surface energy and

Table 1
Thicknesses, FWHM, strain and stress of the *c*-axis, relative peak intensity and crystallite size at various deposition speeds.

Deposition speed (mm/min)	Thickness (μm)	FWHM (°)	Strain of *c*-axis (%)	Stress (GPa)	Relative peak intensity (002)	Crystallite size (nm)
10	0.16	0.343	0.334	−0.78	0.755	26
20	0.18	0.312	0.275	−0.64	0.851	28
30	0.19	0.301	0.217	−0.51	0.882	29
40	0.21	0.282	0.183	−0.43	0.921	31
50	0.22	0.271	0.279	−0.65	0.879	32

tensile strain/compressive stress of the film. The average uniform strain (ε_{zz}) in the lattice along the *c*-axis in the randomly oriented ZnO films was estimated from the lattice parameters using the following expression [36,37]:

$$\varepsilon_{zz} = \frac{c_{film} - c_{bulk}}{c_{bulk}} \times 100\% \tag{3}$$

where c_{film} is the lattice parameter of the strained films calculated from the X-ray diffraction data and c_{bulk} is the lattice parameter of ZnO in the bulk (or powder), i.e., the unstrained lattice parameter. Fig. 3 shows the FWHM and strain values for the ZnO thin films prepared with varying deposition speeds. The FWHM value decreases quasi-linearly as the deposition speed increases. This pattern demonstrates that higher deposition speeds increased the crystallinity of the resulting thin films [38]. Fig. 3 also shows that the strain in the films, ε_{zz}, is tensile. The strain initially decreases from 0.334% to 0.183%, indicating the existence of more relaxed films, and then increases to 0.279% for the deposition speed of 50 mm/min, demonstrating the existence of more tense films [39,40]. These results strengthen the pattern of the XRD results in Fig. 2 and the relative peak intensity (002) reported in Table 1, where the *c*-axis peak first increases and then decreases, suggesting that the higher orientation of the *c*-axis planeis due to the formation of the more relaxed film at a 40 mm/min deposition speed.

A good crystalline quality film can be achieved by the removal of the residual elastic stress due to the small lattice mismatch between ZnO and the glass substrate. The amount of residual stress, σ_{film}, in the ZnO thin film deposited on the glass substrate is derived according to the following equation [41,42]:

$$\sigma_{film} = \frac{2C_{13}^2 - C_{33}(C_{11} + C_{12})}{2C_{13}} . \varepsilon_{zz} \tag{4}$$

where C_{11} = 208.8 GPa, C_{12} = 119.7 GPa, C_{13} = 104.2 GPa andC_{33} = 213.8 GPa are the elastic stiffness constants of bulk ZnO, and ε_{zz} is the average uniform lattice strain along the *c*-axis [43]. This equation yields the following numerical relationship for stress: $\sigma_{film} = -233\varepsilon_{zz}$ (GPa).

Table 1 reports the estimated stress values of the films grown at different deposition speeds. In addition, Fig. 4 shows the relationship between residual stress and the relative (002) peak intensity for the ZnO thin films as a function of deposition speed. The negative sign of stress indicates that the strain is tensile and that the unit cells are under compression. Both intrinsic and extrinsic stress components will affect the resulting stress in the thin films. The impurities, defects and lattice distortions in the crystal structure all influence the intrinsic stress, while the extrinsic stress is influenced by the lattice mismatch and the thermal expansion coefficient mismatch between the film and the substrate. The strain in the films is likely to be of intrinsic rather than thermal origin. The thermal strain introduced by the difference between the linear thermal expansion coefficients, α, of ZnO thin film ($\alpha_{11} = 6.05 \times 10^{-6}\ °C^{-1}$) and the Corning 7740 glass substrate ($\alpha_{33} = 3.30 \times 10^{-6}\ °C^{-1}$) is significantly smaller than the measured strain [44]; this means that the growth process of the ZnO films contributes to the intrinsic stress, which is the dominant stress acting on the films. The strain values calculated in Table 1 indicate that the lattice constant, *c*, of the ZnO thin films is elongated along the unit cell of the*c*-axis. Thus, the compressive force acts on the ZnO thin films as a result of unit cell elongation.

Hur et al. reported that thicker films will normally produce a relaxed extrinsic stress in the thin films, but in this case, the film thickness ranges between 160 and 220 nm [45]. Thus, the extrinsic stress will not be present, and the resulting stress values seem to be dominantly intrinsic, as proven by the calculations. As the deposition speed increases from 10 to 40 mm/min, the compressive stress first decreases to the minimum stress of 0.43 GPa, nearly stress free, and approaches the value of unstressed bulk ZnO before increasing again to 0.65 GPa at 50 mm/min. The reduction in the compressive stress might be due to the enhancement in crystallinity, contributing to a lower occurrence of defects and lattice distortions in the crystal lattice structure [46].

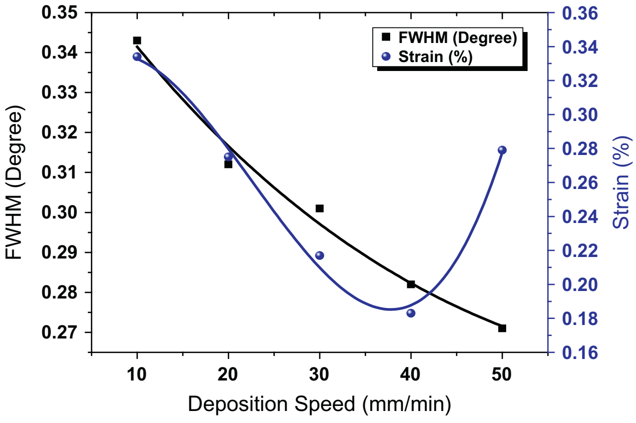

Fig. 3. Variation in the FWHM and strain of the ZnO thin films with various deposition speeds.

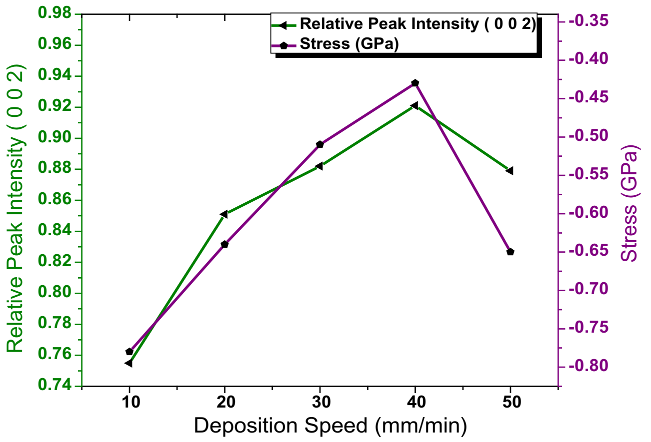

Fig. 4. Variation of the relative (002) peak intensity and stress of the ZnO thin films with deposition speed.

The FESEM morphologies of the ZnO thin films produced at various deposition speeds are shown in Fig. 5 (50 k magnification at 5 kV applied voltage). The average grain size determined from the micrographs increases as the deposition speed increases from 10 mm/min to 50 mm/min. This finding is in agreement with the XRD crystallite size results reported in Table 1. As reported by Numpud et al., the increase in grain size is affected by the deposition speed due to the competitive effects of gravitational and frictional viscous forces acting on the liquid coating film and solvent evaporation [47]. The coated thin films become thicker as the deposition speed of the sol–gel process increases. The relationship between the film thickness (t) and the deposition speed (v) is defined as $t \propto v^{2/3}$ [48]. Therefore, more zinc particles are present in thicker films, increasing the electrostatic interactions between particles. This condition increases the probability that particles congregate together to form a grain. Thus, the grain size increases as the deposition speed is increased. The presence of the nanoparticles is more clearly observed in the film morphology for thicker films. As the deposition speed of the substrate is increased, no sudden changes are observed in the surface morphology of the films, with the exception of an increase in particle size. All of the ZnO thin films exhibit uniform coverage of planar grains with irregular shapes, but the porous structure still prevails (Fig. 5a–e). A compact and less porous surface covered by larger grains is observed when the films are produced at higher deposition speeds.

According to Brinker and Scherer, the thin films become thicker as the deposition speed increases, and the number of Zn^{2+} particles in the films increases [22,48]. Thus, the growth rate of the ZnO thin films will increase at higher deposition speeds. When the film growth is too fast, there is no chance for the arriving material to rearrange into a more definite structure, disturbing the preferred crystal orientation of the films, as discussed in reference to the XRD results. The voids around the grains are reduced at higher deposition speeds and increase the efficiency of physical contact, which in turn decreases the resistivity of the films, as previously reported. Furthermore, the increase in the particle size in the thin film will increase the surface contact between the particles and improve the packing density in the thin films. An increase in particle size at a higher deposition speed can reduce the oxygen adsorption at the grain boundaries, decreasing carrier trapping in thin films, thus decreasing the resistivity. Carrier traps occur when the adsorbed oxygen becomes trapped at the grain boundary, thus increasing the grain boundary potential barrier among the ZnO particles. The potential barrier will prevent the carrier from moving from one particle to another, which will decrease the carrier mobility of the ZnO thin films prepared at lower deposition speeds. This phenomenon will contribute to an increase in the resistivity of the thin film, as discussed in the section above on electrical properties. Nevertheless, the surface contact between ZnO particles can be improved by increasing the deposition speed, leading to the reduction of oxygen, depriving the carrier traps of charged carriers and thus reducing the resistance by decreasing the potential barrier at the grain boundaries [49,50]. Previous reports have noted that the film thickness increases at higher deposition speeds [48]. The film thickness was measured by surface profilometry (KLA Tencor P-6 profilometer) and was found to be in the range of 0.16–0.22 μm. The variation in thickness obtained by the surface profiler is presented in Table 1.

Raman spectroscopy provides information on the vibrational properties of ZnO. ZnO with a hexagonal wurtzite structure is well known to belong to the space group C_{6V}^{4}, with two formula units per primitive cell. Each unit cell contains 4 atoms and occupies 2b sites of symmetry C_{3V} [51]. Group theory predicts that the optical phonons for wurtzite ZnO at the Γ_{opt} point of the Brillouin zone belong to the following irreducible representation (5) [52]:

$$\Gamma_{opt} = A_1 + 2B_1 + E_1 + 2E_2 \tag{5}$$

where both the A_1 and E_1 modes are polar and are split into transverse optical modes (A_1-TO andE_1-TO) resulting from beating in the basal plane and longitudinal optical modes (A_1-LO and E_1-LO) resulting from beating along the c-axis, with different frequencies due to the macroscopic electric fields associated with LO phonons. For lattice vibrations with A_1 and E_1 symmetry, the atoms move parallel and perpendicular to the c-axis, respectively. The A_1 and E_1 branches are both Raman and infrared active. The two non-polar E_2 modes are Raman active only. Only B_1 modes are inactive (silent modes). In the case of highly oriented ZnO films, the incident light was exactly normal to the surface; only the E_2 modes and the A_1-LO mode were expected to emerge, and the other modes were forbidden according to the well-known Raman selection rules [51]. Fig. 6a presents typical Raman spectra of the ZnO films deposited at various deposition speeds. The observed phonon frequencies are E_2 (low) = ~101 cm^{-1}, E_2 (high) = ~437 cm^{-1}, and A_1-LO = ~585 cm^{-1}. These optical phonon modes confirm that these nanocrystalline films contain the wurtzite hexagonal phase.

Some researchers have reported that the E_2 (low) peak can determine the crystallinity of the films and is associated with the vibration of the heavy Zn sublattice [53]. If the E_2 (low) peak is the sharpest and highest intensity peak, then the sample has the best crystal quality. The E_2 (high) mode of ZnO is often related to

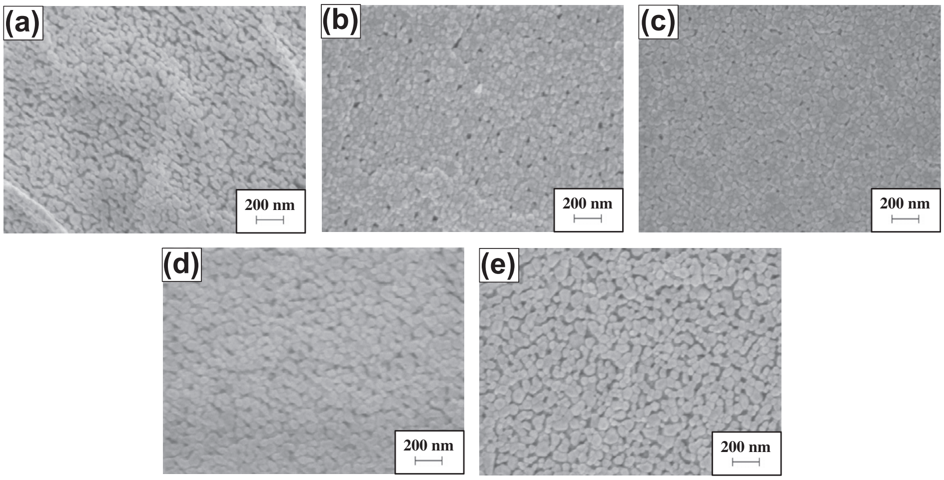

Fig. 5. FESEM morphology of ZnO thin films prepared at various deposition speeds: (a) 10 mm/min, (b) 20 mm/min, (c) 30 mm/min, (d) 40 mm/min and (e) 50 mm/min.

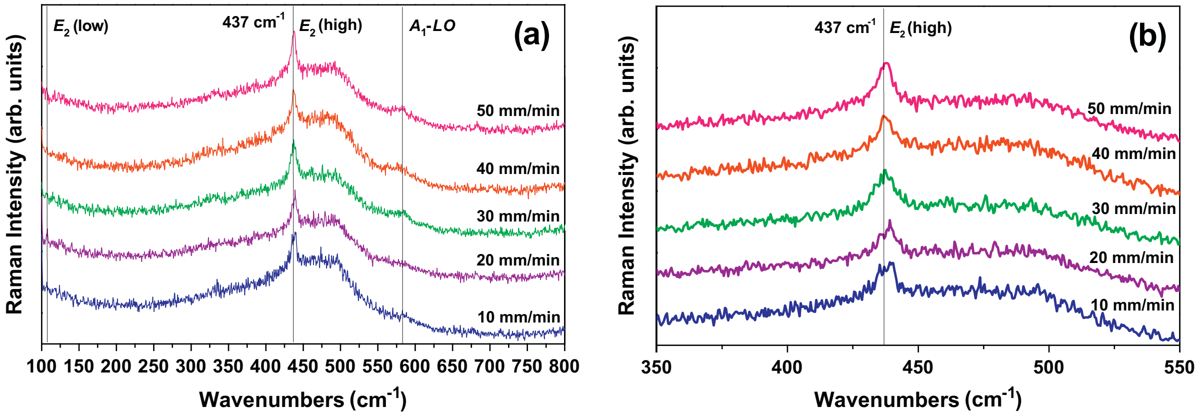

Fig. 6. (a) Raman spectra of ZnO thin films prepared at various deposition speeds and (b) an enlarged view of the signal ranging from 350 to 550 cm^{-1}.

oxygen atoms, and it is shifted due to the intrinsic stress in ZnO films. According to the Raman results, the E_2 (high) peak shift to higher wavenumbers compared with the bulk value of 437 cm^{-1} indicates the existence of a compressive stress in the films, which was confirmed by XRD results [54]. The peak shift can be clearly observed in Fig. 6b, which is indicative of the trend of compressive stress in the ZnO films.

The peak of the A_1-LO mode of ZnO is associated with oxygen deficiency. Some reports assigned this wavenumber as E_1-LO [55]. A_1-LO has often been associated with the wavenumbers of 570 cm^{-1}, 574 cm^{-1}, 579 cm^{-1} and 582 cm^{-1} [56]. According to the theoretical calculation, the A_1-LO theoretical wavenumber is 559 cm^{-1}. A higher wavenumber contribution suggests an improvement in the crystallinity and a reduction in the defects of the ZnO films [57]. TheA_1-LO mode exhibited a very weak intensity, indicating the minimisation of the effect of oxygen deficiency on the growth of strongly *c*-axis-oriented ZnO films. The preparation of ZnO films with a strong *c*-axis orientation will enhance the electron transport in the vertical direction, which is important for light harvesting applications for high performance optical devices such as light emitting diodes (LEDs) and solar cells [58].

3.2. Optical properties

Fig. 7 presents the transmittance spectra of as-grown films in the wavelength range of 300–1500 nm. All ZnO thin films exhibited a high transparency of over 85% in the visible and NIR regions, while the absorption edges were below 400 nm for all ZnO thin films. This finding was attributed to the intrinsic band gap of the ZnO due to electron transitions from the valence band to the conduction band.

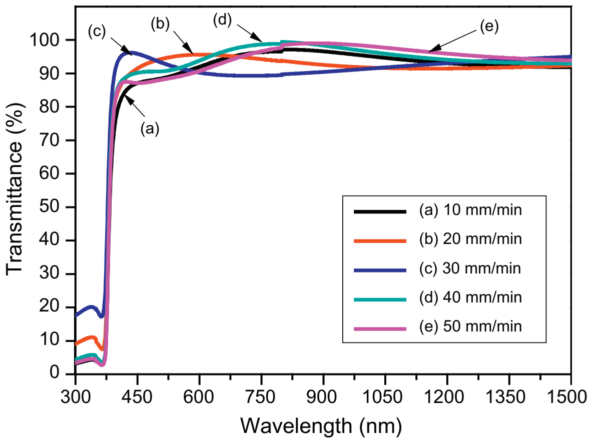

Fig. 7. Transmittance spectra of ZnO thin films prepared at various deposition speeds as a function of wavelength.

The transmission decreased sharply near the ultraviolet region at approximately 380 nm, corresponding to the intrinsic band gap energy of ZnO. The deposition speed had little influence on the pattern of the transmittance spectra. However, the average transmittance in the visible range proved that a higher transmittance (over 90%) is achieved at a lower deposition speed, as shown in Table 2. The lower average transmittance properties of the ZnO thin films prepared at higher deposition speeds may be due to the increases in particle size and film thickness and the presence of voids around the grains, as previously discussed in reference to the FESEM results. At higher deposition speeds (>10 mm/min), the ZnO thin films exhibited a decrease in the optical transmittance due to the formation of larger particles, which may have increased the optical scattering at the grain boundaries. The increase in the film thickness at higher deposition speeds also increased the optical scattering, reducing the transmittance of the thin films. The absorption coefficient, α, can be calculated using Lambert's Law based on relation (6):

$$\alpha = \frac{1}{t}\ln\left(\frac{1}{T}\right) \qquad (6)$$

where t is the thickness of the thin film and T is the transmittance of the thin film. The absorption coefficients of 0.4 M ZnO thin films produced at various deposition speeds are presented in Fig. 8. The spectra reveal an increase in the absorption coefficient in the UV region (<400 nm) as the deposition speed is increased to 40 mm/min. Moreover, the absorption coefficient demonstrates an excitonic nature that becomes more prominent as the deposition speed increases. This effect is attributed to the pattern of strain with increasing deposition speed. The reduction of UV light absorption for the ZnO thin films prepared at a 50 mm/min deposition speed might be due to the formation of higher order defects in the thin

Table 2
Optical properties and porosity of ZnO thin films prepared at various deposition speeds.

Deposition speed (mm/min)	Average transmittance (%)	Optical bandgap energy (eV)	Urbach energy (meV)	Porosity (%)
10	93.99	3.276	86	49.70
20	93.87	3.280	63	49.00
30	91.56	3.283	61	38.10
40	91.47	3.289	60	37.76
50	91.45	3.286	63	37.68

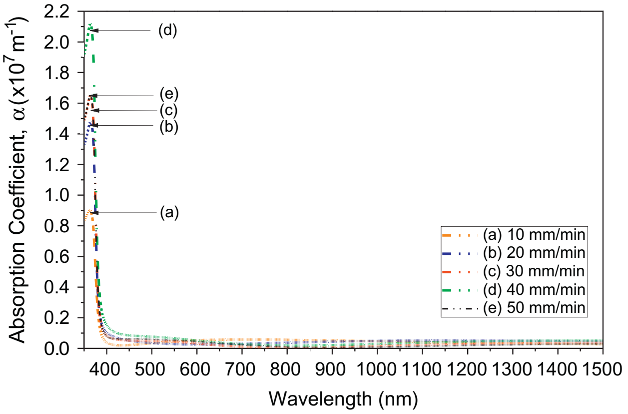

Fig. 8. Absorption coefficient, α, of ZnO thin films prepared at various deposition speeds as a function of wavelength.

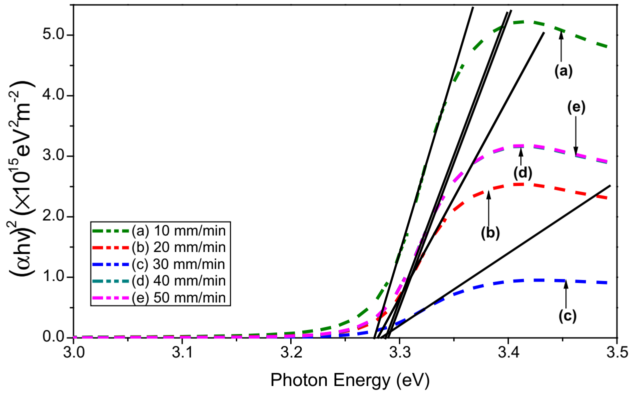

Fig. 9. Estimates of the optical band gap energy, E_g, of ZnO thin films using Tauc's plot as a function of deposition speed.

films as the preferred growth orientation along the c-axis plane decreases [12]. Meanwhile, the absorption coefficient in the visible region (400–800 nm) does not exhibit any significant change with the deposition speed. However, the highest absorption coefficient was observed for the film deposited at 40 mm/min. This result fits with the improvement in the film crystallinity along the preferred c-axis plane, which enhanced the light absorption at the grain boundaries [19]. The optical band gap energy (E_g) values of the films were determined by applying the Tauc model in the high absorption region using the following relations [59,60]:

$$\alpha h\upsilon = B(h\upsilon - E_g)^n \tag{7}$$

$$\alpha h\upsilon = B\sqrt{h\upsilon - E_g} \tag{8}$$

where α is the absorption coefficient, $h\upsilon$ is the photon energy, E_g is the optical band gap and B is an energy-independent constant with values between 1×10^5 and $1 \times 10^6\ \text{cm}^{-1}\ \text{eV}^{-1}$ [60,61]. For $n = 1/2$, the transition data provide the best linear curve in the band edge region, implying that the transition is direct in nature. The absorption coefficient, α, must be assumed to satisfy the equation for a band gap direct material to calculate the band gap energy of the films, as shown in Eq. (7). The optical band gap values, E_g, of the ZnO films were obtained from the transmission measurements by plotting $(\alpha h\upsilon)^2$ versus $h\upsilon$ and extrapolating the linear portion of the absorption edge to find the intercept with the energy axis. Sharp ultraviolet absorption edges at approximately $\lambda = 380$ nm can be observed, with the absorption edge shifted to shorter wavelengths as the deposition speed is increased to 40 mm/min. However, the band edge is shifted to a longer wavelength at a deposition speed of 50 mm/min. The shift in the band edge can be clearly observed in Fig. 9. From the Tauc plot, the estimated optical band gap energy of the ZnO thin films ranged between 3.276 and 3.289 eV, which is in close agreement with the values reported by other researchers for polycrystalline ZnO thin films and with published values for ZnO electronic transition band gap data [62]. The variation in the optical band gap might be due to the optical scattering by grain boundaries and aggregates, which are influenced by the various deposition speeds. The variations in compressive stress and band gap energy, E_g, with deposition speed are shown in Fig. 10. The band gap energy value, E_g, is consistent with the trend in the stress. The stress changes the interatomic spacing of semiconductors, which affects the energy gap [63]. The band gap energy, E_g, increases with increasing tensile stress along the c-axis but decreases with increasing compressive stress [37,64]. The compressive stress in the films leads to a decrease in the band gap. The compressed lattice is expected to provide a narrower band gap because of the decreased repulsion between the zinc 4s and oxygen 2p bands [37], thus explaining the increase in E_g with the decrease in compressive stress as the deposition speed increases.

The absorption coefficient near the fundamental absorption edge exhibits an exponential dependence on the incident photon energy and obeys the empirical Urbach relation. The absorption edge in the spectral range of direct optical transitions has an exponential shape described by the following equation [65]:

$$\alpha = \alpha_o \exp\left(\frac{h\upsilon}{E_u}\right) \tag{9}$$

where α_o is the pre-exponential factor and E_u is known as the Urbach energy, which is the width of the localised state. Taking the natural logarithm of Eq. (9) yields the following equation:

$$\ln\alpha = \ln\alpha_o + \left(\frac{h\upsilon}{E_u}\right) \tag{10}$$

Thus, a plot of $\ln(\alpha)$ versus photon energy, $h\upsilon$, should be linear, with the slope representing the Urbach energy. Fig. 11 presents the Urbach plots of the films. The Urbach energy was calculated from the reciprocal gradient of the linear portion of these curves and is interpreted in Fig. 12. Urbach energy values, E_u, vary inversely with the optical band gap energy, E_g. The Urbach energy first gradually decreases and then increases for deposition speeds exceeding 40 mm/min, thus indicating defect formation. During the formation of these films, some defects are formed that produce localised states in the films. Thus, the increase in the width of the localised states (Urbach energy) decreases the optical band gap energy

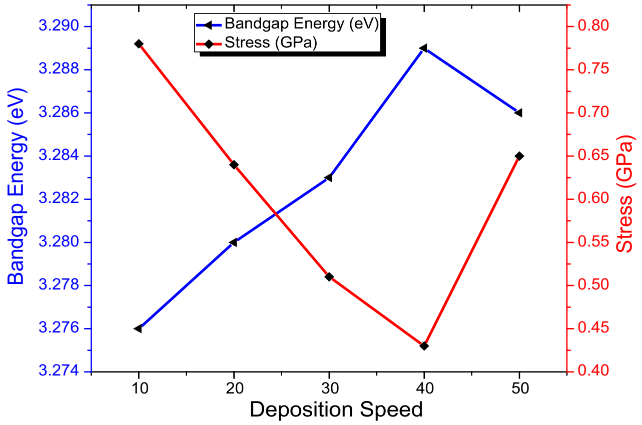

Fig. 10. Variation of the optical band gap energy, E_g, and compressive stress of ZnO thin films as a function of deposition speed.

[66,67]. This effect explains the changes in the *c*-axis orientation pattern as the deposition speed is increased. The porosity of the ZnO thin films has been calculated using the Lorentz–Lorentz equation presented below [21,68]:

$$\text{Porosity} = 1 - \left[\frac{[(n_f^2 - 1)/(n_f^2 + 2)]}{[(n_s^2 - 1)/(n_s^2 + 2)]}\right] \tag{11}$$

where n_f is the refractive index of the porous ZnO film and n_s is the refractive index of the ZnO skeleton, which is widely accepted as 2 [69]. In the transmittance region where the absorption coefficient $\alpha = 0$, the refractive index, n_f, is calculated based on the following equations [70]:

$$n_f = \left[N + (N^2 - s^2)^{1/2}\right]^{1/2} \tag{12}$$

$$N = \frac{2s}{T_m} - \left(\frac{(s^2 + 1)}{2}\right) \tag{13}$$

T_m is the envelope function of the transmittance maxima and minima, while *s* is the refractive index of the substrate, which is typically 1.52 for the totally transparent glass substrate used in this study [71]. The T_m value is obtained by taking the average of the transmittance data from the transparent region, or the region where the α value is close to 0 [39]. Based on the results of this study, this region is between wavelengths of 400 and 800 nm. The porosities calculated for all films are summarised in Table 2. The results in the table suggest that the porosity tends to decrease at higher deposition speeds.

3.3. Photoluminescence

Fig. 13 presents the PL spectra of the ZnO thin films prepared at various deposition speeds. The luminescence of the ZnO thin films is closely related to the film crystallinity because the density of defects in the film decreases as the crystallinity is improved. Room temperature PL emission spectra for all of the films were measured in the wavelength range of 350–700 nm at an excitation wavelength of 325 nm. Generally, ZnO films exhibit two emission peaks, the UV emission and the deep-level emission in the visible range. The PL spectra in all samples exhibit a strong UV emission at the near band edge centred at 380 nm due to free-exciton recombination [72,73]. The UV peak increases with the deposition speed. The intensity increases with increasing deposition speed because the thicker film contains more zinc particles, leading to an increase in the carrier concentration and enhancing the UV emission [74]. A broad visible emission ranging from 520 to 640 nm with a peak located in the yellow range (610 nm) was observed for the deep-level emission in the ZnO thin films and was attributed to structural defects such as oxygen vacancies (V_o^+) and interstitial oxygen (O_i^-) [75,76]. Biaxial strain in ZnO films only affects UV emission and does not change the position or intensity of deep level emission.

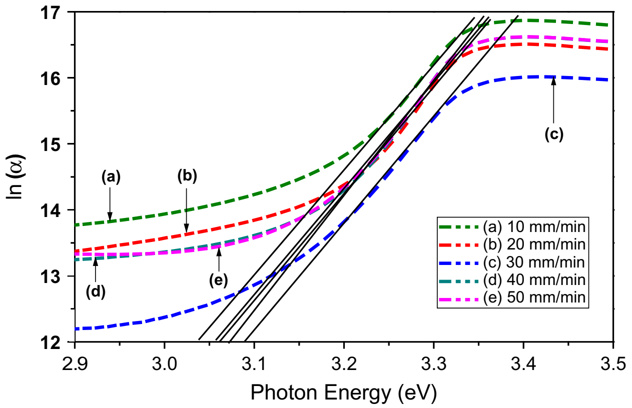

Fig. 11. Plot of ln(α) versus photon energy for ZnO thin films prepared at various deposition speeds.

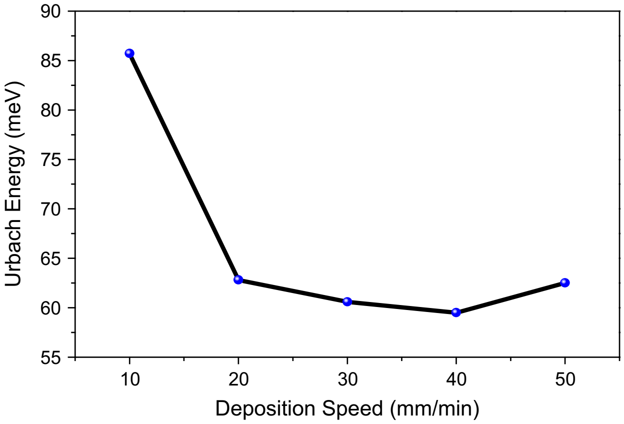

Fig. 12. Urbach energy, E_u, of ZnO thin films as a function of deposition speed.

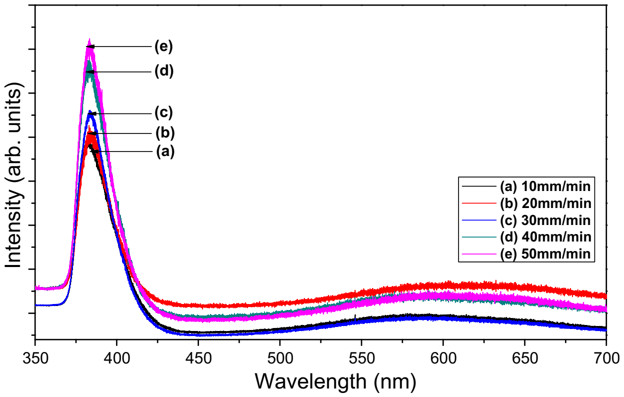

Fig. 13. Photoluminescence spectra of the ZnO thin films as a function of deposition speed.

3.4. Electrical properties

The deposition speed might play an important role in the sheet resistivity of thin films. Therefore, an *I*–*V* characteristic curve of the films prepared at various speeds is plotted in Fig. 14. The resistivity was calculated from the slopes of the linear *I*–*V* plot using the sheet resistivity formula (14) for a thin film:

$$\rho = \left(\frac{V}{I}\right)\frac{wt}{l} \tag{14}$$

where *V* is the supplied voltage, *I* is the measured current, *t* is the film's thickness, *w* is the electrode width and *l* is the length between the electrodes. The conductivity of the film, σ, was determined using the following equation :

$$\sigma = \frac{1}{\rho} \tag{15}$$

The active area of the thin films is 3×10^{-6} m^2. The inset in Fig. 14 shows the variation in resistivity with respect to deposition speed. The *I*–*V* results show that all of the films exhibit ohmic behaviour. The resistivity decreases with increasing deposition speed, and the minimum resistivity was observed for the films deposited at 50 mm/min, while the maximum resistivity was observed for the films prepared at a 10 mm/min deposition speed. A higher deposi-

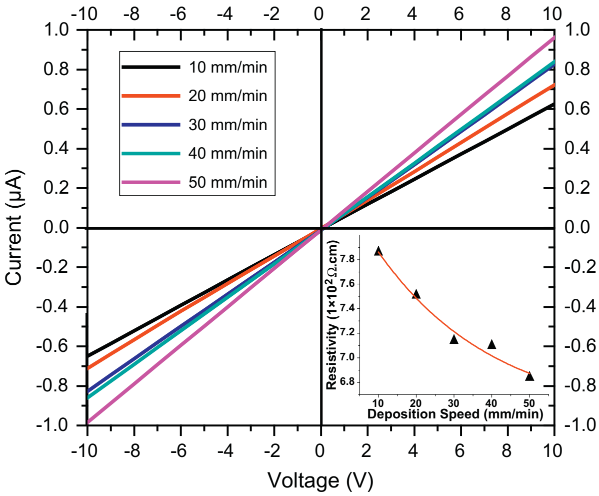

Fig. 14. *I–V* characteristic curves of the ZnO thin films prepared at various deposition speeds. The inset shows the variation in resistivity as a function of deposition speed.

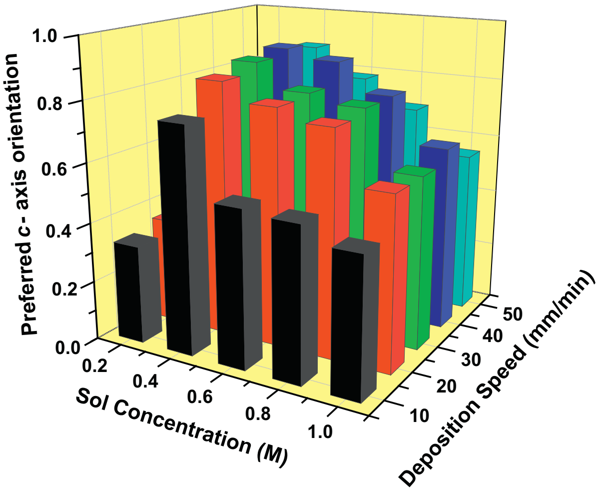

Fig. 15. Response surface/contour diagrams as a function of sol concentration and deposition speed.

tion speed will produce a thicker thin film due to the competitive effects of gravitational and frictional viscous forces acting on the liquid film coating and solvent evaporation [21,23,77]. This evaporation process between the deposition processes increases the sol viscosity, which in turn results in a thicker film [78]. The *I–V* trend suggests that the Zn^{2+} species is present at higher levels in thicker thin films due to the higher deposition speed, which enhances the carrier concentration in thin films [24]. The patterns of resistivity and conductivity are summarised in Table 3.

4. Response surface/contour

Based on our previous paper on sol concentration [19] and the present research on deposition speed, a response surface plot was prepared considering the relative peak intensity as the response. Fig. 15 presents the plot as a function of sol concentration and deposition speed, which enables the optimisation of the preparation of *c*-axis oriented ZnO thin films. The results suggest that the deposition speed has no clear effect on the orientation of the grain growth. Indeed, the XRD analysis shows that the grains were always oriented according to the *c*-axis perpendicular to the substrate surface, regardless of the deposition speed. The oriented grain growth of the (002) plane may occur because of the presence of slightly oriented grains in the previous layer. However, various diffraction peaks were observed for every sol concentration. At higher sol concentrations, the (002) peak decreased with increasing Zn concentration, while the (100), (101), (102) and (110) peaks gradually increased, indicating an increase in the grain boundary density for the thin films. However, the crystallite size was influenced by both parameters, with increases in both parameters leading to increases in the crystallite size. This study of the effects of sol concentration and deposition speed demonstrates that the ZnO thin film prepared at 0.4 M and deposited at 40 mm/min exhibited the highest crystal orientation along the *c*-axis plane.

Table 3
Electrical properties and thicknesses of ZnO thin films prepared at various deposition speeds.

Precursor concentration (M)	Deposition speed (mm/min)	Resistivity, ρ (Ω cm)	Conductivity, σ (S cm^{-1})
0.4	10	7.86×10^2	1.27×10^{-3}
	20	7.51×10^2	1.33×10^{-3}
	30	7.14×10^2	1.40×10^{-3}
	40	7.10×10^2	1.41×10^{-3}
	50	6.84×10^2	1.46×10^{-3}

5. Conclusions

A ZnO film with a highly preferred *c*-axis (002) orientation was obtained at a deposition speed of 40 mm/min by the sonicated sol–gel dip-coating technique. The existence of only one texture in all cases, namely, the *c*-axis texture, shows that the growth orientation of these films is independent of the deposition speed. The crystalline quality of the films improved at 40 mm/min, and corresponding increases in crystallite and grain growth were observed as the deposition speed was increased. Increasing the deposition speed also minimised the strain and stress in the film, which enhanced the electron transport and increased the conductivity due to the shorter carrier pathway. The films deposited at a low deposition speed (10 mm/min) had a large stress (0.78 GPa), which relaxed as the deposition speed was increased. Meanwhile, a nearly stress- and strain-free thin film was obtained for ZnO thin films deposited at 40 mm/min. In addition, the variation of the direct band gap, E_g, was correlated with the compressive stress of ZnO thin films. All of the films exhibited greater than 90% transmittance in the visible region. Furthermore, the electrical resistivity was found to decrease with deposition speed, while the carrier concentration increased with deposition speed, as proven by the PL emission. These results suggest that a suitable deposition speed should be used to obtain higher crystalline and stress-free ZnO thin films for applications in optoelectronic devices such as sensors and solar cells.

Acknowledgements

Mohd Firdaus Malek would like to thank the Research Management Institute (RMI), Universiti Teknologi MARA (UiTM), Malaysia and the Ministry of Higher Education (MOHE), Malaysia for their financial support. The authors would also like to thank the Faculty of Applied Sciences (UiTM) and the Faculty of Mechanical Engineering (UTHM) for the use of their FESEM and XRD facilities, respectively. The authors thank Mrs. Nurul Wahida (UiTM Asst. Science Officer), Mr. Mohd Azlan Jaafar (UiTM technician) and

Mr. Suhaimi Ahmad (UiTM technician) for their kind support of this research.

References

[1] H. Wu, M. Xue, J. Ou, F. Wang, W. Li, J. Alloys Comp. 565 (2013) 85.
[2] H. Li, Z. Zhang, J. Huang, R. Liu, Q. Wang, J. Alloys Comp. 550 (2013) 526.
[3] C. Klingshirm, Phys. Status Solidi B 71 (1975) 547.
[4] J.Y. Lee, J.H. Lee, H.S. Kim, C.H. Lee, H.S. Ahn, H.K. Cho, Y.Y. Kim, B.H. Kong, H.S. Lee, Thin Solid Films 517 (2009) 5157.
[5] J.J. Hassan, M.A. Mahdi, Y. Yusof, H. Abu-Hassan, Z. Hassan, H.A. Al-Attar, A.P. Monkman, Opt. Mater. 35 (2013) 1035.
[6] A.M.K. Dagamseh, B. Vet, F.D. Tichelaar, P. Sutta, M. Zeman, Thin Solid Films 516 (2008) 7844.
[7] C.S. Rout, A.R. Raju, A. Govindaraj, C.N.R. Rao, Solid State Commun. 138 (2006) 136.
[8] A. Fouchet, W. Prellier, B. Mercey, J. Appl. Phys. 100 (2006) 013901.
[9] Z. Charifi, H. Baaziz, A.H. Reshak, Phys. Status Solidi B 244 (2007) 3154.
[10] D. Bao, H. Gu, A. Kuang, Thin Solid Films 312 (1998) 37.
[11] A.M.P. Santos, Edval J.P. Santos, Thin Solid Films 516 (2008) 6210.
[12] S. Suwanboon, Naresuan Univ. J. 6 (2008) 173.
[13] M. Bouderbala, S. Hamzaoui, B. Amrani, Ali H. Reshak, M. Adnane, B. Amrani, T. Sahraoui, M. Zerdali, Physica B 403 (2008) 3326.
[14] K. Ozga, T. Kawaharamura, A.A. Umar, M. Oyama, K. Nouneh, A. Slezak, S. Fujita, M. Piasecki, A.H. Reshak, I.V. Kityk, Nanotechnology 19 (2008) 185709.
[15] A.H. Reshak, J. Ebothe, A. Wojciechowski, W. Kuznik, A. Popeda, Physica E 42 (2010) 1769.
[16] R. Shabannia, H.A. Hassan, Mater. Lett. 98 (2013) 135.
[17] S. Salam, M. Islam, A. Akram, Thin Solid Films 529 (2013) 242.
[18] Q.A. Drmosh, S.G. Rao, Z.H. Yamani, M.A. Gondal, Appl. Surf. Sci. 270 (2013) 104.
[19] M.F. Malek, M.H. Mamat, M.Z. Sahdan, M.Z. Musa, Z. Khusaimi, M. Rusop, Thin Solid Films 527 (2013) 102.
[20] M.F. Malek, M.Z. Sahdan, M.H. Mamat, M.Z. Musa, Z. Khusaimi, S.S. Husairi, N.D. Md Sin, M. Rusop, Appl. Surf. Sci. 275 (2013) 75.
[21] C.J. Brinker, G.W. Scherer, Sol–Gel Science: The Physics and Chemistry of Sol–Gel Processing, Academic Press, New York, 1975. 803.
[22] W.R. Saleh, N.M. Saeed, W.A. Twej, M. Alwan, Adv. Mater. Phys. Chem. 2 (2012) 11.
[23] M. Ohyama, H. Kouzuka, T. Yoko, Thin Solid Films 306 (1997) 78.
[24] D.J. Goyal, C.M. Agashe, B.R. Marathe, M.G. Takwale, V.G. Bhide, J. Mater. Sci. Lett. 11 (1992) 708.
[25] O. Kozák, P. Praus, R. Dvorsk, Chalcogenide Lett. 9 (2012) 413.
[26] M.H. Mamat, Z. Khusaimi, M.M. Zahidi, S.A. Bakar, Y.M. Siran, S.A.M. Rejab, A.J. Asis, S. Tahiruddin, S. Abdullah, M.R. Mahmood, Jpn. J. Appl. Phys. 50 (2011) 06GH04.
[27] S. O'Brien, L.H.K. Koh, Gabriel M. Crean, Thin Solid Films 516 (2008) 1391.
[28] V.R. Shinde, T.P. Gujar, C.D. Lokhande, Sens. Actuat., B 120 (2007) 551.
[29] M.J. Alam, D.C. Cameron, J. Vac. Sci. Technol., A 19 (2001) 1642.
[30] Y. Zhang, H. Zheng, J. Su, B. Lin, Z. Fu, J. Lumin. 124 (2007) 252.
[31] N. Fujimara, T. Nishibara, S. Goto, J. Xu, T. Ito, J. Cryst. Growth 130 (1993) 269.
[32] Xu Linhua, Xiangyin Li, Jun Yuan, J. Nonlinear Opt. Phys. Mater. 17 (2008) 405.
[33] B.D. Cullity, Elements of X-Ray Diffraction, Addison-Wesley Publishing Company, Inc., London, 1978.
[34] M.Z. Sahdan, M.H. Mamat, M. Salina, Z. Khusaimi, U.M. Noor, M. Rusop, Phys. Status Solidi C 7 (2010) 2286.
[35] E.F. Keskenler, M. Tomakin, S. Doğan, G. Turgut, S. Aydın, S. Duman, B. Gürbulak, J. Alloys Comp. 550 (2013) 129.
[36] Selected powder diffraction data for metals and alloys, JCPDS, USA 1, 1978, 108.
[37] R. Ghosh, D. Basak, S. Fujihara, J. Appl. Phys. 96 (2004) 2689.
[38] J.M. Myong, W.H. Yoon, D.H. Lee, I. Yun, S.H. Bae, S.Y. Lee, Jpn. J. Appl. Phys. 41 (2002) 28.
[39] S. Mridha, D. Basak, Mater. Res. Bull. 42 (2007) 875.
[40] B.L. Zhu, X.H. Sun, S.S. Guo, X.Z. Zhao, J. Wu, R. Wu, J. Liu, Jpn. J. Appl. Phys. 45 (2006) 7860.
[41] V. Gupta, A. Mansingh, J. Appl. Phys. 80 (1996) 1063.
[42] X.J. Ping, S.S. Bo, L. Lan, Z.X. Song, W.Y. Xin, C.X. Ming, Chin. Phys. Lett. 27 (2010) 047803.
[43] Y.G. Wang, S.P. Lau, H.W. Lee, S.F. Yu, B.K. Tay, X.H. Zhang, K.Y. Tse, H.H. Hng, J. Appl. Phys. 94 (2003) 1597.
[44] J.H. Jou, M.Y. Han, D.J. Cheng, J. Appl. Phys. 71 (1992) 4333.
[45] T.B. Hur, Y.H. Hwang, H.K. Kim, I.J. Lee, J. Appl. Phys. 99 (2006) 064308.
[46] S.Y. Kuo, W.C. Chen, F.I. Lai, C.P. Cheng, H.C. Kuo, S.C. Wang, W.F. Hsieh, J. Cryst. Growth 287 (2006) 78.
[47] P. Numpud, T. Charinpanitkul, W. Tanthapanichakoon, J. Ceram. Soc. Jpn. 116 (2008) 414.
[48] C.J. Brinker, G.W. Scherer, Sol–Gel Science: The Physics and Chemistry of Sol–Gel Processing, Academic Press, San Diego, Calif, USA, 1990. 788.
[49] M. Boshta, F.A. Mahmoud, M.H. Sayed, J. Avonic Res. 6 (2010) 93.
[50] K. Ogata, K. Sakurai, Sz. Fujita, Sg. Fujita, K. Matsushige, J. Cryst. Growth 214 (2000) 312.
[51] T.C. Damen, S.P.S. Porto, B. Tell, Phys. Rev. B 142 (1966) 570.
[52] C.A. Arguello, D.L. Rousseau, S.P. Porto, Phys. Rev. 181 (1969) 1351.
[53] J.N. Zeng, J.K. Low, Z.M. Ren, T. Liew, Y.F. Lu, Appl. Surf. Sci. 197–198 (2002) 362.
[54] C. Wang, Z. Chen, Y. He, L. Li, D. Zhang, Mater. Sci.-Poland 28 (2010) 153.
[55] X.L. Xu, S.P. Lau, B.K. Tay, Thin Solid Films 398–399 (2001) 244.
[56] J. Ye, S. Gu, S. Zhu, T. Chen, W. Liu, F. Qin, L. Hu, R. Zhang, Y. Shi, Y. Zheng, J. Vac. Sci. Technol., A 21 (2003) 979.
[57] C. Charpentier, P. Prod'homme, I. Maurin, M. Chaigneau, P. Roca i Cabarrocas, EPJ Photovoltaics 2 (2011) 25002.
[58] W.E. Buhro, V.L. Colvin, Nat. Mater. 2 (2003) 138.
[59] J. Tauc, R. Grigorovici, A. Vancu, Phys. Status Solid 15 (1996) 627.
[60] E.A. Davis, N.F. Motta, Philos. Mag. 22 (1970) 903.
[61] S.A.B.S.A. Bux, S.H.A. Aziz, Z.A. Talib, W.M.D.W. Yusoff, Solid State Sci. Technol. 13 (2005) 251.
[62] J. Rodríguez-Báez, A. Maldonado, G. Torres-Delgado, R. Castanedo-Pérez, M. de la L. Olvera, Mater. Lett. 60 (2006) 1594.
[63] J.I. Pankove, Optical Processes in Semiconductors, Dover Publication, New York, 1971. 22.
[64] V. Srikant, D.R. Clarke, J. Appl. Phys. 81 (1997) 6357.
[65] S. Ilican, M. Caglar, Y. Caglar, J. Optoelectron. Adv. Mater. 9 (2007) 1414.
[66] C.I. Oriaku, J.C. Osuwa, C.H. Njoku, J. Non-Oxide Glasses 3 (2011) 25.
[67] A. Meeder, D. Fuertes MarrÓn, A. Rumberg, M.Ch. Lux-Steiner, J. Appl. Phys. 92 (2002) 3016.
[68] J.H. Yim, J.B. Kim, H.D. Jeong, Y.Y. Lyu, S.K. Mah, J.H. Lee, K.H. Lee, S. Chang, L.S. Pu, Y.F. Hu, J.N. Sun, D.W. Gidley, Mater. Res. Soc. Symp. Proc. 766 (2003) E8.10.1.
[69] G. Wypych, Handbook of Fillers, second ed., Chem Tech. Publishing, Canada, 1999. pp. 172.
[70] V. Pandey, N. Mehta, S.K. Tripathi, A. Kumar, J. Optoelectron. Adv. Mater. 7 (2005) 2641.
[71] R. Tricker, Optoelectronics and Fiber Optic Technology, Newnes, Woburn, 2002. pp. 39.
[72] J.C. Johnson, H. Yan, P. Yang, R.J. Saykally, J. Phys. Chem. B 107 (2003) 8816.
[73] L.E. Greene, M. Law, J. Goldberger, F. Kim, J.C. Johnson, Y. Zhang, R.J. Saykally, P. Yang, Angewandte Chemie 115 (2003) 3139.
[74] C.J. Brinker, G.C. Frye, A.J. Hurd, C.S. Ashley, Thin Solid Films 201 (1991) 97.
[75] X.L. Wu, G.G. Siu, C.L. Fu, H.C. Ong, Appl. Phys. Lett. 78 (2001) 2285.
[76] K. Vanheusden, W.L. Warren, C.H. Seager, D.R. Tallant, J.A. Voigt, B.E. Gnade, J. Appl. Phys. 79 (1996) 7983.
[77] P. Yimsiri, M.R. Mackley, Chem. Eng. Sci. 61 (2006) 3496.
[78] L. Landau, B. Levich, Acta Physicochim., URSS 17 (1942) 42.